1D Hierarchical $MnCo_2O_4$ Nanowire@MnO_2 Sheet Core–shell Arrays on Graphite Paper as Superior Electrode for Asymmetric Supercapacitor

Shude Liu[a], K.S. Hui[b,*], K.N. Hui[c,*]

[a]Department of Materials Science and Engineering, Pusan National University, San 30 Jangjeon-dong, Geumjeong-gu, Busan 609-735, Republic of Korea.

[b]Department of Mechanical Convergence Engineering, Hanyang University, 17 Haengdang-dong, Seongdong-gu, Seoul 133-791, Republic of Korea.

[c]Institute of Applied Physics and Materials Engineering, University of Macau, Avenida da Universidade, Taipa, Macau, China.

[*]*Corresponding author:*

E-mail: kshui@hanyang.ac.kr (K.S. Hui)

Tel: +82 2-2220-0441; Fax: +82 2-2220-2299

E-mail: bizhui@umac.mo (K.N. Hui)

Tel: +853 8822-4426; Fax: +853 8822-2426

Keywords: Heterostructure; Core–shell; $MnCo_2O_4$ nanowire; MnO_2 sheet; Asymmetric supercapacitor

Abstract

Heterostructured metal oxides core–shell architectures have attracted considerable attention owing to their superior electrochemical performance in supercapacitors compared to a single structure. Here, we report a simple and effective synthesis of hierarchical $MnCo_2O_4$ nanowire@MnO_2 sheet core–shell nanostructures anchored on graphite paper for use in supercapacitors. The proposed electrode exhibites a specific capacitance of 2262 F g^{-1} at 1 A g^{-1}. In addition, good rate capability and excellent cycling performance are observed. An asymmetric supercapacitor with operating potential at 1.6 V is demonstrated using $MnCo_2O_4$@MnO_2 as cathode and graphene/nickel foam (NF) as anode. The $MnCo_2O_4$@MnO_2//graphene/NF asymmetric device shows a high energy density of 85.7 Wh kg^{-1} at a power density of 800 W kg^{-1} while maintaining a high energy density of 34.7 Wh kg^{-1} at 24 kW kg^{-1}. Moreover, the device demonstrates a long-term cycling stability of 81.6% retention of its initial specific capacitance.

Introduction

Many studies have focused on the development of high-performance electrochemical energy storage devices to address the increasing energy demand and environmental deterioration.[1] Supercapacitors, a promising device for electrochemical energy storage, have attracted significant research attention in recent years because of their overall advantages over electrostatic capacitors and batteries in terms of their high power density, long lifespan, rapid charge/discharge rates, safe operation, and environmental friendliness.[2] On the other hand, the relative energy density of carbonaceous compound-based electrodes have hindered their applications in real

energy devices.[3] Alternative pseudocapacitor materials, including conducting polymers and transition metal oxides, have showed higher energy densities.[4] In particular, conducting polymers have a high energy density but low cycling stability.[5] In the search for high performance electrode materials available for supercapacitors, binary metal oxides have shown great promise as an alternative for supercapacitor electrodes because of the advantages of achievable mixed valences, and high electrical conductivity relative to single component oxides,[6] such as $NiCo_2O_4$,[7] $MnCo_2O_4$,[8] $CuCo_2O_4$,[9] $ZnMn_2O_4$,[10] and $CoMoO_4$.[11] $MnCo_2O_4$, in particular, has attracted considerable interest in supercapacitor applications owing to its high availability, low-cost and environmental friendliness.[8] More significantly, $MnCo_2O_4$ has demonstrated excellent capacitive behaviour and high rate capability in supercapacitors because cobalt has a higher oxidation potential, while manganese can assume multiple oxidation states and bring in higher rate capacity.[8] For example, Xu et al. synthesized porous $MnCo_2O_4$ nanowires as a pseudocapacitor electrode in a 2 M KOH aqueous solution, which exhibited a discharge capacitance of 1342 F g^{-1} at 1 A g^{-1}.[12] Xia et al. produced $Co_xMn_{3-x}O_4$ nanorods and hollow octahedrons composites from a simple hydrothermal method that displayed a capacitance of 266.8 F g^{-1} at 5 mV s^{-1} with good cycling performance (80.2 % remaining after 1000 cycles) for supercapacitor applications.[13] Wu et al. reported flower-like $CoMn_2O_4$ microsphere architectures that showed a specific capacitance of 188 F g^{-1} at 1 A g^{-1} in a 1M Na_2SO_4 solution with good cycling stability by retaining 93% of its original capacitance after 1000 cycles.[14]

Lightweight, low-cost, flexible supercapacitors with the capability of rapidly storing a high energy density is an increasing trend towards portable electronics that is effectively levelling the cyclic features of renewable energy sources. Currently,

commercial supercapacitors have suffered from drawbacks, such as (1) they can be oxidized under ambient conditions, (2) have poor bend-ability, and (3) heavy weight of the conductive substrates (nickel foam or copper foam), which have severely limited the energy density of the overall electrode. In contrast, graphite paper is not only highly conductive, but is also lightweight, low-cost, bendable, and inert under ambient conditions. In addition, it can be woven to form wearable cloths,[15] which is attractive as an electrode material for flexible supercapacitors. In addition, active electrochemical materials, such as $NiCo_2O_4$,[7] NiCoAl−LDH/NiCo−carbonate hydroxide[15] and MnO_x/CNT/RGO,[3a] have shown enhanced energy and power densities after been grown directly on graphite paper, resulting in not only good mechanical adhesion and electrical connection, but also avoiding the use of polymer binders or conductive additives.

Recently, nanomaterials, particularly one-dimention core–shell heterostructures, have proven to be an effective strategy for utilizing active materials in supercapacitors due to the following advantages: Core–shell structure provides more active sites for desirable electron transport pathways not only at the active materials surface but also throughout the bulk. The open-network and free interspaces among these nanowire arrays can be efficiently utilized, which shorten ion diffusion paths and improve the utilization rate of electrode materials.[16] In addition, the synergistic combination of the virtues of the individual components for rich Faradaic redox reactions. For example, Zou et al. reported mesoporous $NiCo_2O_4$@MnO_2 core–shell nanowire arrays as an electrode showing a specific capacitance of 112 F g^{-1} at 1 mA cm^{-2}.[16] Huang et al. reported core−shell ellipsoidal $MnCo_2O_4$ showing a large initial charge capacity of 1433.3 $mAhg^{-1}$ at 0.1 A g^{-1}.[17] Zhang et al. synthesized a hierarchical

$ZnCo_2O_4$@MnO_2 core–shell nanotube array electrode exhibiting a high areal capacitances of 2.38 F cm^{-2} at 6 mA cm^{-2}.[18] On the other hand, there have been few studies of the electrochemical capacitance of hierarchical heterostructured $MnCo_2O_4$ nanowires@MnO_2 nanosheets ($MnCo_2O_4$@MnO_2) core–shell architectures, even though the individual capacitive properties of both have been investigated extensively.

In the present study, a new electrode design strategy was exploited to fabricate integrated, binder-free and lightweight hierarchical $MnCo_2O_4$@MnO_2 core–shell arrays anchored on functionized graphite paper as cathode electrode in supercapacitor. MnO_2 nanosheets were coated onto needle-like $MnCo_2O_4$ nanowire arrays as a backbone on a flexible graphite paper support. The resulting hierarchical self-supported $MnCo_2O_4$@MnO_2 core–shell arrays electrode delivered a high specific capacitance of 2262 F g^{-1} and 1103 F g^{-1} at current densities of 1 A g^{-1} and 20 A g^{-1}, respectively, which are superior to those of the $MnCo_2O_4$ electrode at the same current density. Moreover, the $MnCo_2O_4$@MnO_2 electrode also demonstrated good cycling stability and showed an 87.1 % initial capacitance retention after 5000 cycles at 10 A g^{-1}. An asymmetric supercapacitor (ASC) fabricated with $MnCo_2O_4$@MnO_2 and graphene/NF exhibited a cell voltage of 1.6 V with a specific capacitance of 241 F g^{-1} at current density of 1 A g^{-1}, and maintained a high specific capacitance of 98 F g^{-1} at high current density of 30 A g^{-1}. Moreover, The ASC device delivered a high energy density of 85.7 Wh kg^{-1} at a power density of 800 W kg^{-1}. In addition, the ASC device showed good stability towards long-term charge–discharge tests (81.6% retention after 8000 cycles). The present $MnCo_2O_4$@MnO_2 heterostructure with remarkable electrochemical properties makes it a potential electrode material for the next generation high energy density supercapacitors.

Experimental

Preparation of functionalized graphite paper

All chemicals were used as purchased. The graphite paper was cleaned several times with acetone, ethanol and deionized water, and dried at room temperature. According to previous reports,[19] graphite paper was functionalized via an electrochemical corrosion method in a solution of 2 M H_2SO_4. A typical three-electrode configuration measurement was conducted with graphite paper as the working electrode, platinum sheet as the counter electrode and saturated calomel electrode (SCE: Hg/Hg_2Cl_2) as the reference electrode. A constant voltage of 2.2 V was maintained for 20 min during the corrosion process. Subsequently, the functionalized graphite paper was obtained

Synthesis of hierarchical structure of $MnCo_2O_4$ nanowire arrays

Hierarchical structure $MnCo_2O_4$@MnO_2 nanowires were synthesized by combining a hydrothermal reaction and a thermal annealing process. In a typical synthesis procedure, $Mn(NO_3)_2{\cdot}4H_2O$ (2 mmol), $Co(NO_3)_2{\cdot}6H_2O$ (4 mmol), urea (24 mmol), and ammonium fluoride (10 mmol) were dissolved in deionized water (70 mL) with vigorous magnetic stirring. After stirring for 1 h, the as-obtained solution was transferred to a 100 mL Teflon container, and a piece of the functional graphite paper substrate was then immersed into the reaction solution. The autoclave was sealed and maintained at 120 ℃ for 5 h in an electric oven. After cooling naturally to room temperature, the products on the graphite paper were carefully washed several times with deionized water and absolute ethanol with ultrasonication, and then dried overnight at 60 ℃. Subsequently, the samples were calcined at 300 ℃ for 2 h at a

ramping rate of 2 ℃ min^{-1} to transform the $MnCo_2O_4$ precursor to hierarchical structured $MnCo_2O_4$ nanowires.

Synthesis of hierarchical structure of $MnCo_2O_4$@MnO_2 core–shell arrays

The $MnCo_2O_4$@MnO_2 core–shell structure was synthesised by a direct redox reaction between the carbon and $KMnO_4$. During thermal annealing, the $MnCo_2O_4$ precursor was transformed to a $MnCo_2O_4$ nanowire, whereas carbon layer was coated on the surface of the $MnCo_2O_4$ nanowire from the evaporation of graphite paper. Carbon layer anchored to the surface of the $MnCo_2O_4$ nanowire works as a reducing agent to reduce the $KMnO_4$ to MnO_2 nanosheets coated on the surface of the $MnCo_2O_4$ nanowire. In the process, the $MnCo_2O_4$ nanowire coated with carbon on graphite paper was dispersed in 35 mL of a 0.02 M $KMnO_4$ solution and underwent a hydrothermal process at 120℃ for 2 h. After cooling naturally to room temperature, the products on the graphite paper were washed carefully with deionized water and absolute ethanol with ultrasonication and then dried at 50 °C for 10 h. For comparison, samples of $MnCo_2O_4$ nanowires grown on functionalized graphite paper were obtained under the same conditions without adding $KMnO_4$. In order to decrease the uncertainty of the mass of the electrode, we prepared an active material on functionlazed graphite paper with the size of 2×4 cm^2. Then, the total mass loadings of $MnCo_2O_4$ and $MnCo_2O_4$@MnO_2 on the graphite paper were 6.52 and 15.49 mg, respectively.

Materials characterization

The chemical composition and crystallite phase of the as-synthesized products were characterized by X−ray diffraction (XRD, D8−Discovery, Brucker) analysis using Cu

Kα radiation (λ=1.54 Å) at an accelerating voltage and current of 40 kV and 200 mA, respectively. The XRD patterns were obtained over the range, 10~80°(2θ), at a scanning speed of 0.2°/s. The microstructure and morphology were examined by scanning electron microscopy (SEM, Hitachi S−4800) and high resolution transmission electron microscopy (HR-TEM, JEOL, JEM−2010F). The valence state of the prepared samples was determined by X−ray photoelectron spectroscopy (XPS, VG Scientifics ESCALAB250), which was calibrated to the carbon peak C 1s at 284.6 eV.

Electrochemical measurement

The electrochemical performance was measured on an IVIUM electrochemical workstation system (Ivium, nState) using a three-electrode mode in a 6 M KOH solution. The reference electrode and counter electrode were SCE and platinum, respectively. Heterostructured $MnCo_2O_4$@MnO_2 core–shell array electrode materials or pristine $MnCo_2O_4$ electrode materials supported on the graphite paper were used directly as the working electrode. The electrochemical tests of the ASC device were performed on a two-electrode cell with $MnCo_2O_4$@MnO_2 electrode as positive electrode and graphene/NF as negative electrode in a 6 M KOH aqueous electrolyte solution. The CV curves were measured in the potential range between 0 and 0.5 V at different scan rates from 2 to 50 mV s^{-1}. The galvanostatic charge/discharge processes were performed by cycling the potential from 0 to 0.4 V at a range of current densities (1, 2, 3, 4, 5, 8, 10, and 20 A g^{-1}). The cycling stability was evaluated by a charge/discharge process at a current density of 10 A g^{-1} for more than 5000 cycles over the voltage range, 0 to 0.4 V. The EIS data was collected over the frequency

range of 100 KHz to 0.01 Hz by applying an AC voltage with a 5 mV perturbation at the open circuit potential.

Results and discussion

Fig. 1 presents the fabrication process for the hierarchical $MnCo_2O_4$@MnO_2 core–shell arrays on graphite paper as supercapacitor electrode materials. First, graphite paper was functionalized with oxygen functional groups, such as carbonyl, hydroxyl and carboxylic (step 1). The $MnCo_2O_4$ precursor ((Co, Mn)OOH is shown in the Fig. S1) nanowires were grown on functionalized graphite paper via a hydrothermal process (step 2). During the thermal annealing process, the (Co, Mn)OOH nanowires were transformed to $MnCo_2O_4$ nanowires, whereas carbon layer was coated on the surface of the $MnCo_2O_4$ nanowires (step 3). Finally, $MnCo_2O_4$@MnO_2 arrays were obtained by growing MnO_2 nanosheets onto the surface of the $MnCo_2O_4$ nanowires via a second hydrothermal method. In a previous report, the growth of a MnO_2 shell on active core materials was achieved by the impregnation of a glucose aqueous solution and subsequent post-annealing in Ar gas to produce an amorphous carbon layer on the active material surface, which acted as the carbon precursor for reduction of $KMnO_4$ to MnO_2 by a chemical reaction between $KMnO_4$ and graphitic carbon ($4MnO_4^- + 3C + H_2O = 4MnO_2 + CO_3^{2-} + 2HCO_3^-$).[20] In the present study, the growth of a MnO_2 shell on the active materials was achieved by utilizing the graphite paper as the carbon source, in which a thin layer of carbon was coated on the surface of the $MnCo_2O_4$ nanowires during the thermal annealing process of the graphite paper. The porous MnO_2 nanosheets were then grown directly on the surface of the $MnCo_2O_4$ nanowires arrays by dispersing $MnCo_2O_4$ nanowires arrays in 35 mL of a

0.02 M $KMnO_4$ solution and underwent a hydrothermal process at 120℃ for 2 h, forming high surface area heterostructured core–shell nanostructures, making them fully available for the efficient Faradiac redox reaction. To verify the role of carbon layer for reduction of $KMnO_4$ to MnO_2 on the surface of $MnCo_2O_4$ nanowires arrays, $MnCo_2O_4$ nanowires arrays grown on Ni foam were put in 35 mL of a 0.02 M $KMnO_4$ solution and underwent the same hydrothermal process. Fig. S2 (Supplementary Information) shows the SEM images of the (Co, Mn)OOH (Fig. S2a-b), $MnCo_2O_4$ nanowires arrays (Fig. S2c-d) and $MnCo_2O_4$ nanowires arrays after second hydrothermal growth in $KMnO_4$ solution on Ni foam (Fig. S2e-f). Results showed clearly that MnO_2 shell did not form on the surface of the $MnCo_2O_4$ nanowires arrays, confirming the importance of the carbon layer for reduction of $KMnO_4$ to MnO_2 on the surface of $MnCo_2O_4$ nanowires arrays.

The crystal phase of the $MnCo_2O_4$@MnO_2 structure was analysed by XRD, as shown in Fig. 2a. All the diffraction peaks of the $MnCo_2O_4$ nanowires were indexed to the JCPDS card no. 1-1130. Moreover, the characteristic peaks located at 21.8°, 28.0°, 35.1°, 36.8°, and 42.1° 2θ were assigned to the (101), (201), (301), (210), and (002) planes of the MnO_2 (JCPDS card no. 39-375), respectively, confirming the existence of the $MnCo_2O_4$@MnO_2 heterostructure by this approach. The detailed microstructures of the $MnCo_2O_4$@MnO_2 arrays were examined by TEM.

Fig. 2b and c shows the XPS spectrum of the $MnCo_2O_4$@MnO_2 core–shell structure, which were calibrated with reference to the C 1s peak at 284.6 eV. The Mn 2p XPS spectrum revealed three kinds of manganese species that were assigned to species containing Mn^{2+}, Mn^{3+} and Mn^{4+} ions (Fig. 2b). In particular, the fitting peaks at

binding energies of 641.5 and 653.4 eV were ascribed to Mn^{2+}, whereas the peaks at 643.5 and 654.5 eV were assigned to Mn^{3+}.[21] Moreover, the Mn 2p spectrum was best fitted to two major peaks at binding energies of 654.4 and 642.6 eV with a spin-energy separation of 11.8 eV, which was assigned to Mn^{4+}.[22] Similarly, the Co 2p emission spectrum (Fig. 2c) was best fitted with two spin-orbit doublets, which could be observed at 780.5 and 795.8 eV, respectively, demonstrating the presence of both Co^{2+} and Co^{3+} species.[23] In addition, the synthetic effects of the MnO_2 shell and $MnCo_2O_4$ core provide not only richer redox couples, $Mn^{4+}/Mn^{3+}/Mn^{2+}$ and Co^{3+}/Co^{2+}, but also many electroactive sites in the $MnCo_2O_4$@MnO_2 structures, which is beneficial to the long-term cycling stability and high rate capacity of the $MnCo_2O_4$@MnO_2 electrode.

SEM and TEM were used to examine the structure and morphology of the as-prepared materials. As shown in a low-magnification SEM image in Fig. 3a and b, the (Co, Mn)OOH nanowires with a needle-like shape were grown densely on the graphite paper surfaces. A close observation of the nanowire showed that the individual (Co, Mn)OOH nanowires have a mean diameter of approximately 50 nm and a length of up to several microns (Fig. 3c). After calcination at 300℃ for 2 h in air (Fig. 3d-f), wiregrass-like $MnCo_2O_4$ nanowires preserved the original morphology with a similar length and dimensions. Fig. 3g shows that the as-prepared $MnCo_2O_4$@MnO_2 arrays were grown uniformly over surface of the graphite paper with a mean diameter of approximately 135 nm and lengths of around several microns. High-magnification SEM showed that highly dense MnO_2 nanosheets were grown uniformly over the surfaces of the $MnCo_2O_4$ nanowires backbone and closely connected to each other to form a continuous open-network structure (Fig. 3h and i). The existence of graphite

paper supporter was verified by the Fig. S3. Such a design has several advantages: (1) the nanosheets allow for a short diffusion length of ions and maintain the structural integrity of the core during the charge/discharge process; (2) the 1D nanowires serve as both the backbone and electron superhighway for charge transport; and (3) the interconnected open-network core–shell features leading to huge exposed surface areas between the electrode and electrolyte lead to the efficient utilization of electrode materials, thus contributing to a high specific capacitance;[24]

Fig. 4 presents TEM images of the $MnCo_2O_4$@MnO_2 structure. The surfaces of the $MnCo_2O_4$ nanowires were covered uniformly by thin interconnected sheet-like subunits with a thickness of approximately several nanometres, as confirmed by the TEM images in Fig. 4a. Fig. 4b shows that $MnCo_2O_4$ nanowire possesses a porous structure with wormhole-like nanopores, which were attributed to nanopores generated as H_2O and gases were released from the decomposition of precursors by thermal annealing. Siginificantly, the nanopores structure can allow the efficient diffusion of electrolyte ions. Moreover, within such unique hierarchical core–shell nanowires, the open and free interspaces among these $MnCo_2O_4$ nanowires arrays can be utilized efficiently, which will allow easier access of the electrolyte ions to the surface of the active materials and improve the utilization rate of the electrode materials. Therefore, a high electrochemical performance resulting from a $MnCo_2O_4$@MnO_2 structure is expected. Furthermore, the selected area electron diffraction (SAED) pattern of the MnO_2 nanosheets confirmed the single-crystalline nature (Fig. 4c), which corresponds to the planes of ramsdellite-type MnO_2 (JCPDS 39-375), as shown in the XRD data. The HRTEM image of the $MnCo_2O_4$ core (Fig. 4d) showed that the d-spacing of 0.204 nm corresponds to the distance of the (400)

plane of the $MnCo_2O_4$ nanowire crystal, whereas the MnO_2 nanosheet showed a lattice spacing of 0.225 nm, which corresponds to the (311) interplanar spacing of MnO_2. Energy-dispersive X-ray spectroscopy (EDS) of the individual sample further revealed O, Co and Mn distributed uniformly over the structure (Fig. 4e). The corresponding EDS element maps showed that Co was located mostly in the inner areas of the core–shell architecture, whereas Mn and O were distributed in the entire regions, confirming the hierarchical core–shell structure of $MnCo_2O_4$@MnO_2.

To demonstrate the electrochemical superiority of the proposed heterostructured $MnCo_2O_4$@MnO_2 electrode, electrochemical studies of the electrode were conducted in a three-electrode configuration using a 6 M KOH solution as the electrolyte with Pt and Hg/HgO as the counter and reference electrodes, respectively. Fig. 5a shows the comparison of CV curves of $MnCo_2O_4$, $MnCo_2O_4$@MnO_2 to the background signal from the graphite paper over a potential window between 0 and 0.5 V at a scan rate of 10 mV s^{-1}. The typical curve exhibited obvious pseudocapacitance features with one pair of well-defined redox peaks, suggesting that the capacitance characteristics are controlled by a reversible Faradaic redox reaction, which is very different from that of carbon with a rectangular CV curve. It should be noted that the graphite paper has negligible contribution to the capacitance of the whole electrode (about 7.84 % for $MnCo_2O_4$ samples and 5.29 % for $MnCo_2O_4$@MnO_2 samples). The CV integrated area of the $MnCo_2O_4$@MnO_2 electrode was apparently larger than that of the $MnCo_2O_4$, indicating that the $MnCo_2O_4$@MnO_2 electrode has a significantly larger specific capacitance than the unitary $MnCo_2O_4$ electrode. The CV curves of the $MnCo_2O_4$ nanowires (Fig. 5b) revealed an anodic peak at approximately 0.24 V and the cathodic peak at 0.14 V, which were assigned to oxidation on Co^{2+}/Co^{3+} and

reduction on Mn^{3+}/Mn^{4+} through the possible electrochemical reactions reported earlier.[25] The CV curves of the $MnCo_2O_4$@MnO_2 electrode (Fig. 5c) revealed a pair of redox reaction peaks at 0.35 V and 0.2 V, which resulted mainly from redox reactions related to M–O/M–O–ON, where M represents Co or Mn ions and N represents H or K ions.[16, 26] A similar shift of the redox reaction peaks to lower and higher potential ends was reported in $ZnCo_2O_4$@MnO_2 core–shell structure.[18] Compared to the CV curves of $MnCo_2O_4$, the area integrated within the CV curve of $MnCo_2O_4$@MnO_2 electrode was higher than that of the $MnCo_2O_4$ electrode, suggesting a much higher pseudocapacitance. It is noteworthy to point out that variations in redox peak positions of these two samples, which can be ascribed to the difference in the polarization behaviour and the Ohmic resistance of the electrodes during the CV tests.[27] Interestingly, the shape retention of the CV curves, even at a high scan rate of 50 mV s^{-1} with only a slight shift in the redox peaks due to electrode polarization, indicated that the $MnCo_2O_4$@MnO_2 electrode is in favour of fast redox reactions and possesses better reversibility.[28] An almost linear relationship for the $MnCo_2O_4$ and $MnCo_2O_4$@MnO_2 electrodes was observed between the cathodic peak current density and the square root of the applied scan rate, as shown in Fig. 5d, indicating that the electrochemical reactions in the electrodes are controlled by the diffusion process of OH^- ion and surface redox reactions taking place in the charge storage process. Specifically, the apparent diffusion coefficient (D) of OH^- ion is calculated in prepared materials employing Randles–Sevcik equation,[29]

$$I_p = 2.69\times10^5 \times n^{\frac{3}{2}} \times A \times \sqrt{D} \times Co \times \sqrt{v} \quad (1)$$

$$D(MnCo_2O_4 @ MnO_2)/D(MnCo_2O_4) = [(I_p/\sqrt{v})(MnCo_2O_4 @ MnO_2)/(I_p/\sqrt{v})(MnCo_2O_4]^2$$

$$= (12.6946/11.5785)^2 = 1.202 \quad (2)$$

where I_p is the peak current, n is the number of electrons involved in the reaction, A is the surface area of the electrode, D is the diffusion coefficient of the electrode material, Co is the proton concentration and ν is the scanning rate. The diffusion coefficient of the $MnCo_2O_4$@MnO_2 composite electrode ($D_{MnCo2O4@MnO2}$) was 1.202 time larger than that of the $MnCo_2O_4$ electrode ($D_{MnCo2O4}$), confirming the faster diffusion of OH^- and protons, and the decrease in electrode polarization in the host materials for higher electrochemical behaviour.[30]

Fig. 6a shows the galvanostatic discharge/charge (GCD) curves for the $MnCo_2O_4$ and $MnCo_2O_4$@MnO_2 electrodes at the same current density of 1 A g^{-1}. As expected, the $MnCo_2O_4$@MnO_2 electrode showed a much longer discharging time than that of the $MnCo_2O_4$ electrode. This means that the $MnCo_2O_4$@MnO_2 electrode material exhibits a higher specific capacitance than the $MnCo_2O_4$ electrode material. The GCD curves (Fig. S4, Supplementary Information) of the $MnCo_2O_4$ electrode at different current densities from 1 to 20 A g^{-1} show a deviation from the typical triangular shape of the EDLCs indicating the Faradaic characteristics of charge storage. The shoulders in the charge-discharge graphs at 0.3 V during charging and 0.2 V during discharging indicate the redox reactions, which are consistent with the CV curves. For the $MnCo_2O_4$ electrode, specific capacitances of 1575, 1442, 1299, 1228, 1171, 1036, 923,776, and 685 F g^{-1} at current densities of 1, 2, 3, 4, 5, 8, 10, 15, and 20 A g^{-1} were obtained. The $MnCo_2O_4$@MnO_2 electrode delivered a high pseudocapacitance of 2262, 1906, 1734, 1604, 1503, 1374, 1278, 1181, and 1103 A g^{-1} at current densities of 1, 2, 3, 4, 5, 8, 10, 15, and 20 A g^{-1}, respectively. The GCD curves (Fig. 6b) of the $MnCo_2O_4$@MnO_2 electrode showed a similar shape to that of the $MnCo_2O_4$ electrode but with a slightly elevated discharge/charge plateau, which is consistent with the CV

curves. Remarkably, the capacitance of the $MnCo_2O_4$@MnO_2 electrode outperforms than that of the $MnCo_2O_4$ electrode at various discharge/charge rates (Fig. 6c). The specific capacitance retention was 48.8 % for the $MnCo_2O_4$@MnO_2 electrode compared to 43.5 % for the $MnCo_2O_4$ electrode when the current density was increased from 1 to 20 A g^{-1}, which indicates the efficient utilization of the underlying $MnCo_2O_4$ nanowires despite being covered by the MnO_2 nanosheets. Furthermore, the specific capacitance of the $MnCo_2O_4$@MnO_2 electrode was much higher than those previously reported for directly-grown pseudocapacitive materials, such as $MnCo_2O_4$ nanowires (1342 F g^{-1} at 1 A g^{-1}),[12] $MnCo_2O_4$ nanowire@reduced graphene oxide (334 F g^{-1} at 1 A g^{-1}),[30a] Mn–Ni–Co ternary oxide nanowires (638 F g^{-1} at 1 A g^{-1}),[31] carbon-modified MnO_2 nanosheet (638 F g^{-1} at 0.25 mA cm^{-2}),[32] and MnO_2 nanosheet@graphene (267 F g^{-1} at 0.2 A g^{-1}) [1]. On the other hand, the present $MnCo_2O_4$@MnO_2 heterostructured nanowires showed higher capacitance than other core–shell nanostructures, such as $CuCo_2O_4$ nanowire@MnO_2 nanoflake (327 F g^{-1} at 1.25 F g^{-1}),[33] ZnO@Co_3O_4 core–shell nanowires (857.7 F g^{-1} at 1 A g^{-1}) [34], hierarchical CuO nanotube@MnO_2 nanosheet (276 F g^{-1} at 0.6 F g^{-1}),[22] Ni_3S_2 nanorod@$Ni(OH)_2$ nanosheet (1037.5 F g^{-1} at 5.1 F g^{-1}),[35] and $NiCo_2O_4$@NiS nanoplate (926 F g^{-1} at 6.15 F g^{-1}),[36] etc. Such high pseudocapacitor at large current densities highlights the great advantages of the present core–shell architecture. The superior electrochemical properties of the proposed $MnCo_2O_4$@MnO_2 electrode are explained as follow: (1) core–shell structure provides more active sites for efficient electrolyte ion transportation not only on the surface of active materials but also throughout the bulk; (2) the open-network and free interspaces among these nanowire arrays can be efficiently utilized, which facilitate the electrolyte ions access the surface of active materials more easily and improve the utilization rate of electrode

materials;[16] (3) the enhanced electrochemical performance could be attributed to the synergistic effects of two different components;[27b] (4) 1D nanowire core serves as an efficient backbone for charge transport[24], while 2D shell provides a high surface area for short diffusion paths of ions and maintains the structural integrity of the core during the charge/discharge process; (5) cobalt has a higher oxidation potential, while manganese has multiple oxidation states leading to higher rate capacity.[8]

The electrochemical stability of the $MnCo_2O_4$@MnO_2 electrode was examined by cycling processes. As shown in Fig. 6d, the cycling stability was enhanced largely in the core–shell heterostructure. The overall capacitance loss for $MnCo_2O_4$ was approximately 19.9 % after 5000 cycles, whereas it was only 12.9 % after 5000 cycles for the $MnCo_2O_4$@MnO_2 electrode. Therefore, the proposed heterostructured nanowire arrays electrode have potential excellent electrochemical stability for long cycle life applications at high current densities. Such intriguing capacitive behaviour was attributed to the unique 1D hierarchical core–shell nanowires arrays configuration and the synergistic pseudocapacitive contributions from the $MnCo_2O_4$ nanowires core and the ultrathin MnO_2 sheets shell. Fig. 6e presents the GCD curves of the as-fabricated $MnCo_2O_4$@MnO_2 electrode for the last 6 cycles. Even after a long period of the 5000 GCD tests, the results showed that the as-fabricated electrode maintained good electrochemical reversibility with approximately 98.7 % Coulombic efficiency and remained undistorted and essentially symmetrical. Fig. 6f shows the CV curves of the $MnCo_2O_4$@MnO_2 electrode before and after 5000 cycles at 5 mV s^{-1}. A slight decrease in the integrated area of the CV curves of the two electrodes indicates the long−term stability of $MnCo_2O_4$@MnO_2 electrode.

To further evaluate the electrochemical behaviour, EIS was carried out to reveal the kinetics of the $MnCo_2O_4$@MnO_2 electrode. EIS was performed over the frequency range, 100 kHz to 0.01 Hz. Fig. S5 presents the Nyquist plots of the $MnCo_2O_4$ and $MnCo_2O_4$@MnO_2 electrodes at the open circuit potential. All the Nyquist plots show typical electrochemical capacitor behaviour with a semicircle in the high frequency region, which indicates charge transfer resistance between the electrolyte and the electrode interface. The inset of Fig. 5 clearly showed that the $MnCo_2O_4$@MnO_2 electrode has a lower equivalent series resistance (R_s) of 0.30 Ω compared to that of the $MnCo_2O_4$ electrode (0.48 Ω). Moreover, the $MnCo_2O_4$@MnO_2 electrode also showed a smaller charge transfer resistance, R_{ct}, of 3.71 Ω, than that of the $MnCo_2O_4$ electrode (5.52 Ω), which suggests a lower internal resistance and charge transfer resistance of the $MnCo_2O_4$@MnO_2 electrode. That is important for high electrochemical activity for energy storage.[37]

To evaluate the feasibility of such $MnCo_2O_4$@MnO_2 core–shell electrode, an ASC device is assembled by using $MnCo_2O_4$@MnO_2 as a positive electrode materials and graphene coating on the porous nickel foam (graphene/NF) as the negative electrode. Significantly, the optimal mass ratio of positive and negative electrodes was fixed to 0.32, which is based on the charge balance between the two electrodes (Fig. S6, Supporting Information). A series of CV measurements of $MnCo_2O_4$@MnO_2//graphene/NF ASC device in different voltage windows at 50 mV s^{-1} were carried out to estimate the best operating potential (Fig. 7a). With an increase of the operating potential to 1.6 V, a slight hump can be observed, indicating some irreversible reactions happen when potential window higher than 1.6V.[38] CV curves of the ASC device at different scan rates ranging from 5 to 50 mV s^{-1} were given in

Fig. 7b. The consistent CV curves of ASC device at various scan rates exhibit a combination of both pseudocapacitive and electric double-layer types of capacitance. Galvanostatic charge/discharge curves showed nonlinear lines, indicating the pseudocapacitacne behaviour of the electrode materials (Fig. 7c). The specific capacitance was calculated to be approximately 241, 204, 197, 185, 174, 156, 145,126,114, and 98 F g^{-1} at current densities of 1, 2, 3, 4, 5, 8, 10, 15, 20, and 30 A g^{-1}, respectively (based on the total mass of the active material in the positive and negative electrodes), showing a good rate capability (Fig. 7d). The Nyquist plot of the $MnCo_2O_4$@MnO_2//graphene/NF ASC device was shown in Fig. S7. The equivalent series resistance of the ASC device is around 1.02 Ω, with a slight charge transfer resistance of 0.74 Ω. The results indicate an good ion transport properties of the $MnCo_2O_4$@MnO_2 core–shell electrode.

Schematic diagram of the ASC device was illustrated using the $MnCo_2O_4$@MnO_2 on the graphite paper electrode as the cathode and the graphene on Ni foam as the anode in a 6 M KOH, and a piece of cellulose paper was used as the separator (Fig. 8a). Long term cycling stability is also a critical parameter for practical application of supercapacitors. The cycling was performed using charge/discharge test at current density of 10 A g^{-1} up to 8000 cycles (Fig. 8b). The $MnCo_2O_4$@MnO_2//graphene/NF ASC device shows an outstanding cycling stability and demonstrates 81.6% of the specific capacitance retention (comparing with the second cycle). Moreover, The charge/discharge curves of the initial 10 cycles were shown in the inset of Fig. 8b, from which the discharge curve is almost identical with its corresponding charge counterpart (Fig. S8), implying that an excellent electrochemical reversibility and Coulombic efficiency of the device. To further illustrate the energy and power

properties of the present devices, Ragone plot was plotted derived from charge/discharge data as shown in the Fig. 8c. The $MnCo_2O_4$@MnO_2//graphene/NF ASC device showed a maximum energy density of 85.7 Wh kg^{-1} at a power density of 800 W kg^{-1}, while it maintained a high energy density of 34.7 Wh kg^{-1} at a power densityof 24 kW kg^{-1}. The results showed a much enhanced energy density at high power density as compared with previously reported ASC devices such as a-$Co(OH)_2$@Co_3O_4//AC (13.5 Wh kg^{-1} at 145 W kg^{-1}),[39] $CoMoO_4$@3Dgraphene//AC (21.1 Wh kg^{-1} at 300 W kg^{-1}),[40] $NiCo_2O_4$@MnO_2//AC (35 Wh kg^{-1} at 163W kg^{-1}),[16] $NiCo_2O_4$–rGO//AC (23.3 Wh kg^{-1} at 324.9 W kg^{-1}),[41] (MnNiCo) oxide//C (29 Wh kg^{-1} at 188 W kg^{-1}),[31] Ni_xCo_{3-x} oxide//AC (37.4 Wh kg^{-1} at 163 W kg^{-1}),[38] $Ni(OH)_2$@MnO_2@rGO//rGO (54 Wh kg^{-1} at 392 W kg^{-1}),[42] graphene@MnO_2/graphene (25.2Wh kg^{-1} at 100 W kg^{-1}).[43] Obviously, the exceptional energy density property of $MnCo_2O_4$@MnO_2//graphene/NF ASC device might be related to the advantageous merit of core-shell structure. It is noted that the interconnected MnO_2 nanosheets building blocks grown on $MnCo_2O_4$ nanowire arrays give rise to a highly porous morphology, which provides more active sites for efficient electrolyte ion access not only at the active materials surface but also throughout the bulk. To further demonstrate the potential application of the present ASC device, two devices were connected in series to power a red light-emittingdiode (Fig. 8d).

Conclusions

In summary, 1D hierarchical $MnCo_2O_4$ nanowire@MnO_2 nanosheet core–shell nanowire arrays were fabricated using a facile and cost-effective strategy for supercapacitor applications. The results showed that this heterostructured electrode displays a high specific capacitance of 2262 F g^{-1} at a discharge current density of 1 A g^{-1} (~ 0.4 fold increase in specific capacitance with respect to the pristine $MnCo_2O_4$ nanowire arrays). In addition, this 1D hierarchical heterostructured electrode exhibited good long-term cycling stability at a high charge–discharge current density of 10 A g^{-1} (~ 87.1 % of its initial specific capacitance was retained after 5000 cycles), which were better than those of the pure $MnCo_2O_4$ nanowire arrays. The improved performence indicates a desired structure derived from a synergistic contribution from the $MnCo_2O_4$ nanowire core and MnO_2 nanosheet shell. An ASC device based on $MnCo_2O_4$@MnO_2//graphene/NF configuration was demonstrated to deliver high specific energy densities at various power densities. The asymmetric supercapacitor showed a high energy density of 85.7 Wh kg^{-1} at a power density of 800 W kg^{-1} and 34.7 Wh kg^{-1} at a high power density of 24 kW kg^{-1}. Moreover, the ASC device exhibited an outstanding cycling life of 81.6% of its initial specific capacitance after 8000 cycling.

Acknowledgements

This study was supported by the Basic Science Research Program through the National Research Foundation of Korea (NRF) funded by the Ministry of Education, Science and Technology (2013R1A1A2007365 and 2014R1A1A2055740).

References

[1] L. Peng, X. Peng, B. Liu, C. Wu, Y. Xie, G. Yu, *Nano letters* **2013**, *13*, 2151-2157.

[2] aZ. Wu, X.-L. Huang, Z.-L. Wang, J.-J. Xu, H.-G. Wang, X.-B. Zhang, *Scientific reports* **2014**, *4*; bL. Li, Z. Wu, S. Yuan, X.-B. Zhang, *Energy & Environmental Science* **2014**, *7*, 2101-2122.

[3] aZ. J. Han, D. H. Seo, S. Yick, J. H. Chen, K. K. Ostrikov, *NPG Asia Materials* **2014**, *6*, e140; bZ.-L. Wang, D. Xu, H.-G. Wang, Z. Wu, X.-B. Zhang, *Acs Nano* **2013**, *7*, 2422-2430; cZ.-L. Wang, D. Xu, H.-X. Zhong, J. Wang, F.-L. Meng, X.-B. Zhang, *Science Advances* **2015**, *1*, e1400035.

[4] B. Anasori, M. Beidaghi, Y. Gogotsi, *Materials Today* **2014**, *17*, 253-254.

[5] Z. Zhang, X. Chen, P. Chen, G. Guan, L. Qiu, H. Lin, Z. Yang, W. Bai, Y. Luo, H. Peng, *Advanced Materials* **2014**, *26*, 466-470.

[6] Y. Zhang, L. Li, H. Su, W. Huang, X. Dong, *Journal of Materials Chemistry A* **2015**, *3*, 43-59.

[7] G. Zhang, X. W. D. Lou, *Advanced Materials* **2013**, *25*, 976-979.

[8] A. K. Mondal, D. Su, S. Chen, A. Ung, H. S. Kim, G. Wang, *Chemistry-A European Journal* **2015**, *21*, 1526-1532.

[9] A. Pendashteh, M. S. Rahmanifar, R. B. Kaner, M. F. Mousavi, *Chemical Communications* **2014**, *50*, 1972-1975.

[10] R. K. Sharma, G. Singh, P. Ahuja, *J Mater Chem A* **2015**.

[11] D. Guo, H. Zhang, X. Yu, M. Zhang, P. Zhang, Q. Li, T. Wang, *J Mater Chem A* **2013**, *1*, 7247-7254.

[12] Y. Xu, X. Wang, C. An, Y. Wang, L. Jiao, H. Yuan, *Journal of Materials Chemistry A* **2014**, *2*, 16480-16488.

[13] H. Xiaomin, W. Long, C. Xia, H. Yu, G. Caizhen, X. Ying, W. Ning, *Journal of Materials Chemistry A* **2014**, *2*, 13103-13108.

[14] L. Ren, J. Chen, X. Wang, M. Zhi, J. Wu, X. Zhang, *RSC Advances* **2015**, *5*, 30963-30969.

[15] J. Yang, C. Yu, X. Fan, J. Qiu, *Advanced Energy Materials* **2014**, *4*.

[16] K. Xu, W. Li, Q. Liu, B. Li, X. Liu, L. An, Z. Chen, R. Zou, J. Hu, *J Mater Chem A* **2014**, *2*, 4795-4802.

[17] G. Huang, S. Xu, Z. Xu, H. Sun, L. Li, *ACS applied materials & interfaces* **2014**, *6*, 21325-21334.

[18] W. Ma, H. Nan, Z. Gu, B. Geng, X. Zhang, *Journal of Materials Chemistry A* **2015**, *3*, 5442-5448.

[19] H. Jin, Z. Peng, W. Tang, H. Chan, *RSC Advances* **2014**, *4*, 33022-33028.

[20] J. Liu, J. Jiang, C. Cheng, H. Li, J. Zhang, H. Gong, H. J. Fan, *Advanced Materials* **2011**, *23*, 2076-2081.

[21] L. Li, F. He, S. Gai, S. Zhang, P. Gao, M. Zhang, Y. Chen, P. Yang, *CrystEngComm* **2014**, *16*, 9873-9881.

[22] M. Huang, Y. Zhang, F. Li, Z. Wang, N. Hu, Z. Wen, Q. Liu, *Scientific reports* **2014**, *4*.

[23] X.-F. Lu, D.-J. Wu, R.-Z. Li, Q. Li, S.-H. Ye, Y.-X. Tong, G.-R. Li, *J Mater Chem A* **2014**, *2*, 4706-4713.

[24] D. Dubal, O. Ayyad, V. Ruiz, P. Gómez-Romero, *Chemical Society Reviews* **2015**, *44*, 1777-1790.

[25] N. Padmanathan, S. Selladurai, *Ionics* **2014**, *20*, 479-487.

[26] L. Yu, G. Zhang, C. Yuan, X. W. D. Lou, *Chemical Communications* **2013**, *49*, 137-139.
[27] aY. Chen, B. Qu, L. Hu, Z. Xu, Q. Li, T. Wang, *Nanoscale* **2013**, *5*, 9812-9820; bH. Y. Wang, F. X. Xiao, L. Yu, B. Liu, X. W. D. Lou, *small* **2014**, *10*, 3181-3186.
[28] G. Nie, X. Lu, J. Lei, Z. Jiang, C. Wang, *J Mater Chem A* **2014**, *2*, 15495-15501.
[29] S. G. Krishnan, M. Reddy, M. Harilal, B. Vidyadharan, I. I. Misnon, M. H. Ab Rahim, J. Ismail, R. Jose, *Electrochimica Acta* **2015**, *161*, 312-321.
[30] aJ. Li, E. Shangguan, D. Guo, M. Tian, Y. Wang, Q. Li, Z. Chang, X.-Z. Yuan, H. Wang, *Journal of Power Sources* **2014**, *270*, 121-130; bG. Zhang, T. Wang, X. Yu, H. Zhang, H. Duan, B. Lu, *Nano Energy* **2013**, *2*, 586-594.
[31] L. Li, Y. Zhang, F. Shi, Y. Zhang, J. Zhang, C. Gu, X. Wang, J. Tu, *ACS applied materials & interfaces* **2014**, *6*, 18040-18047.
[32] Y. Huang, Y. Li, Z. Hu, G. Wei, J. Guo, J. Liu, *J. Mater. Chem. A* **2013**, *1*, 9809-9813.
[33] Q. Wang, J. Xu, X. Wang, B. Liu, X. Hou, G. Yu, P. Wang, D. Chen, G. Shen, *ChemElectroChem* **2014**, *1*, 559-564.
[34] D. Cai, H. Huang, D. Wang, B. Liu, L. Wang, Y. Liu, Q. Li, T. Wang, *ACS applied materials & interfaces* **2014**, *6*, 15905-15912.
[35] W. Zhou, X. Cao, Z. Zeng, W. Shi, Y. Zhu, Q. Yan, H. Liu, J. Wang, H. Zhang, *Energy & Environmental Science* **2013**, *6*, 2216-2221.
[36] Q. Chu, W. Wang, X. Wang, B. Yang, X. Liu, J. Chen, *Journal of Power Sources* **2015**, *276*, 19-25.
[37] C. Dong, Y. Wang, J. Xu, G. Cheng, W. Yang, T. Kou, Z. Zhang, Y. Ding, *Journal of Materials Chemistry A* **2014**, *2*, 18229-18235.
[38] X. Wang, C. Yan, A. Sumboja, P. S. Lee, *Nano Energy* **2014**, *3*, 119-126.
[39] M. Jing, Y. Yang, Y. Zhu, H. Hou, Z. Wu, X. Ji, *Electrochimica Acta* **2014**, *141*, 234-240.
[40] X. Yu, B. Lu, Z. Xu, *Advanced Materials* **2014**, *26*, 1044-1051.
[41] X. Wang, W. S. Liu, X. Lu, P. S. Lee, *Journal of Materials Chemistry* **2012**, *22*, 23114-23119.
[42] H. Chen, S. Zhou, L. Wu, *ACS applied materials & interfaces* **2014**, *6*, 8621-8630.
[43] J. Cao, Y. Wang, Y. Zhou, J.-H. Ouyang, D. Jia, L. Guo, *Journal of Electroanalytical Chemistry* **2013**, *689*, 201-206.

Figure captions

Fig. 1 Schematic diagram for the synthesis and morphology of the $MnCo_2O_4$@MnO_2 core–shell structure. Step (1): the surface functional groups (e.g., carbonyl, −hydroxyl, carboxylic, etc) modification of graphite paper by electrochemical process. Step (2): synthesis of the (Co, Mn)OOH on the graphite substrate by a hydrothermal method. Step (3): phase transformation of (Co, Mn)OOH to $MnCo_2O_4$ nanowires onto the graphite substrate and the formation of a carbon coating on the surface of the $MnCo_2O_4$ nanowires during the thermal annealing process. Step (4): grafting of the MnO_2 nanosheet to $MnCo_2O_4$ nanowires backbone by the second hydrothermal method.

Fig. 2 (a) XRD of the $MnCo_2O_4$@MnO_2 core–shell arrays on graphite paper. XPS spectra of the $MnCo_2O_4$@MnO_2 nanowires, (b) Mn 2p region, (c) Co 2p region.

Fig. 3 SEM images of (a-c) (Co, Mn)OOH. (d-f) $MnCo_2O_4$ nanowire arrays. (g-i) $MnCo_2O_4$@MnO_2 core–shell arrays.

Fig. 4 (a and b)TEM images of hierarchical mesoporous $MnCo_2O_4$@MnO_2 core–shell. (c) SAED pattern of the MnO_2 shell. (d) HRTEM image of $MnCo_2O_4$ core. (e) Elemental mapping images of O, Co, and Mn.

Fig. 5 (a) Comparison of CV curves of the $MnCo_2O_4$ nanowire and $MnCo_2O_4$@MnO_2 electrodes and graphite paper at a current density of 10 mV s^{-1}. (b and c) CV curves of the $MnCo_2O_4$ and $MnCo_2O_4$@MnO_2 electrodes at different scan rates. (d) Linear relationship between the cathodic peak current and the square root of the scan rate.

Fig. 6 (a) Comparison of the CD curves of the $MnCo_2O_4$ and $MnCo_2O_4$@MnO_2 electrodes at a current density of 1 A g^{-1}. (b) Charge and discharge curves of the

$MnCo_2O_4$@MnO_2 electrode at different current densities. (c) Specific capacitances of the as-synthesized electrode materials at different current densities. (d) Cycling performance of the $MnCo_2O_4$ and $MnCo_2O_4$@MnO_2 electrodes at 10 A g^{-1}. (e) Charge-discharge curves of the last 6 cycles of the $MnCo_2O_4$@MnO_2 electrode. (f) CV curves of the $MnCo_2O_4$@MnO_2 electrode measured before and after 5000 cycles charge−discharge test at 5 mV s^{-1}.

Fig. 7 (a and b) CV curves of the $MnCo_2O_4$@MnO_2//graphene/NF-ASC device at different voltage windows and different scan rates, respectively. (c and d) CD curves and specific capacitances of the ASC device at different current densities.

Fig. 8 (a) Schematic illustration of the ASC device configuration. (b) Cycling stability of the $MnCo_2O_4$@MnO_2//graphene/NF-ASC device. (c) Ragone plot of the energy density and power density at different current densities of the ASC device. (d) A circuit diagram showing that two ASC devices connected in series can light up an red LED indicator.

Fig. 1

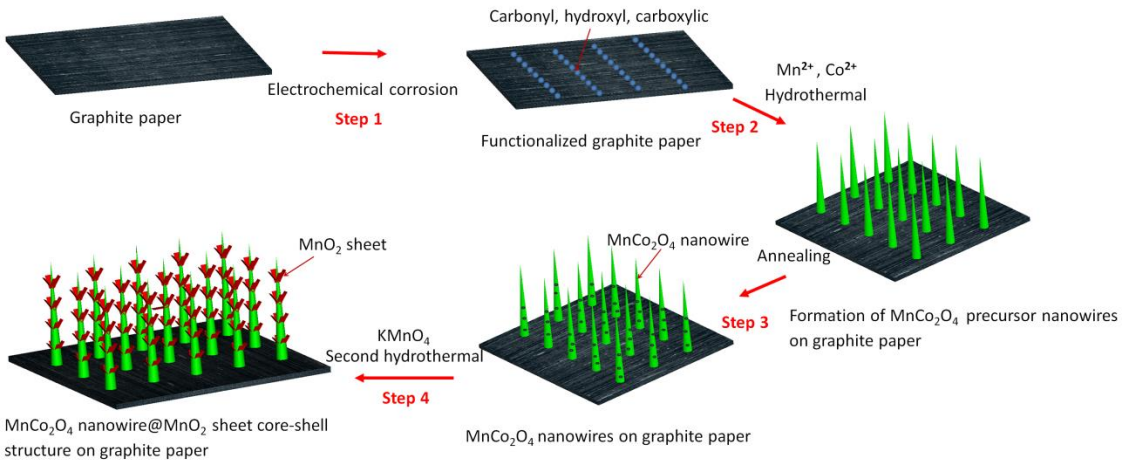
Graphite paper
Electrochemical corrosion
Step 1
Carbonyl, hydroxyl, carboxylic
Functionalized graphite paper
Mn2+, Co2+
Hydrothermal
Step 2
Annealing
Formation of MnCo2O4 precursor nanowires on graphite paper
Step 3
MnCo2O4 nanowire
MnCo2O4 nanowires on graphite paper
KMnO4
Second hydrothermal
Step 4
MnO2 sheet
MnCo2O4 nanowire@MnO2 sheet core-shell structure on graphite paper

1 Fig. 2

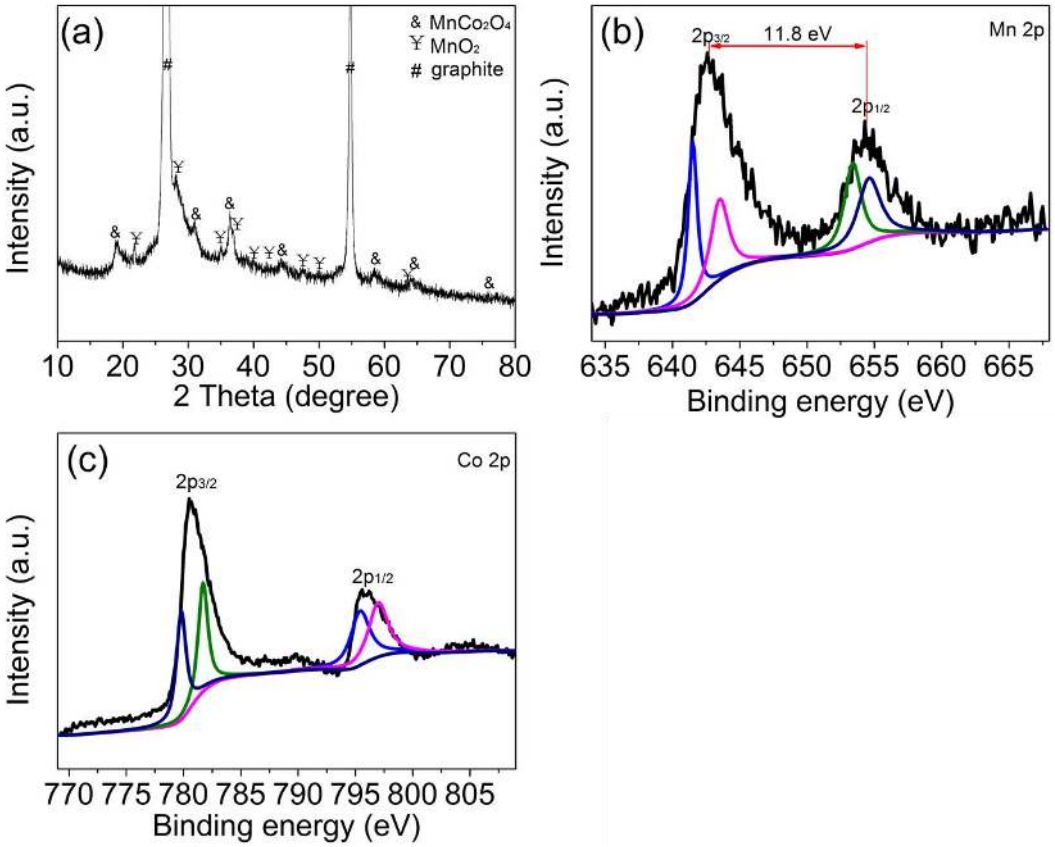
(a)
& $MnCo_2O_4$
ϒ MnO_2
graphite
Intensity (a.u.)
2 Theta (degree)
(b)
$2p_{3/2}$
11.8 eV
$2p_{1/2}$
Mn 2p
Intensity (a.u.)
Binding energy (eV)
(c)
$2p_{3/2}$
$2p_{1/2}$
Co 2p
Intensity (a.u.)
Binding energy (eV)

2
3

Fig. 3

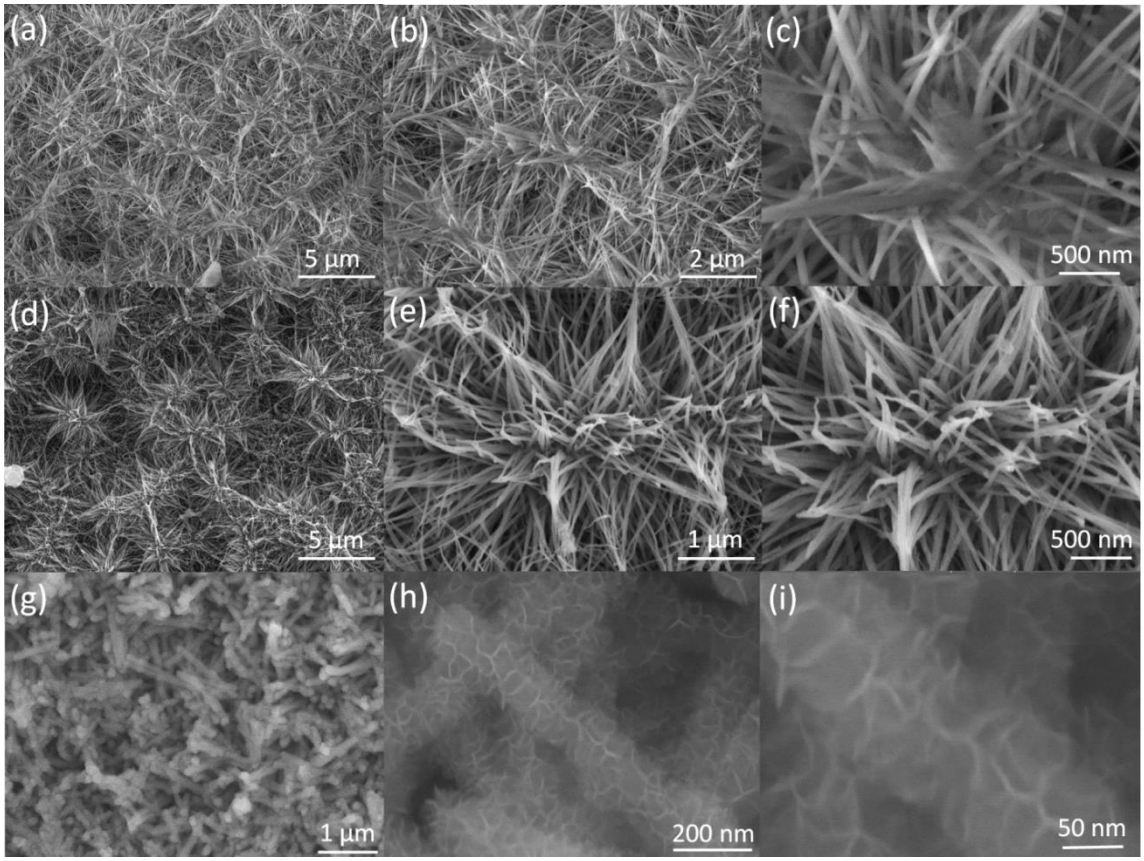

1 Fig. 4

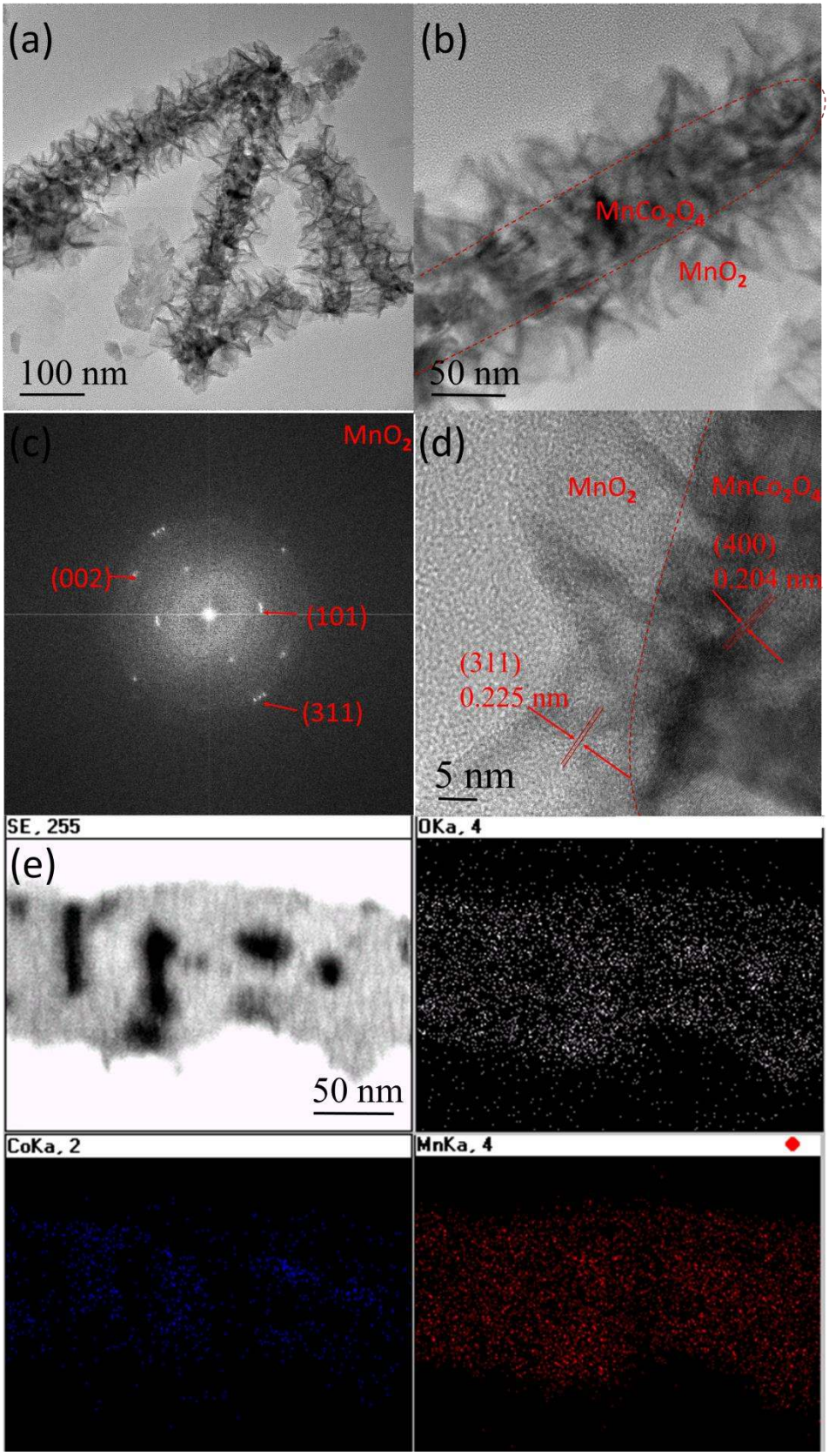
(a)
100 nm
(b)
$MnCo_2O_4$
MnO_2
50 nm
(c)
MnO_2
(002)
(101)
(311)
(d)
MnO_2
$MnCo_2O_4$
(400)
0.204 nm
(311)
0.225 nm
5 nm
SE, 255
OKa, 4
(e)
50 nm
CoKa, 2
MnKa, 4

2

1 Fig. 5

2

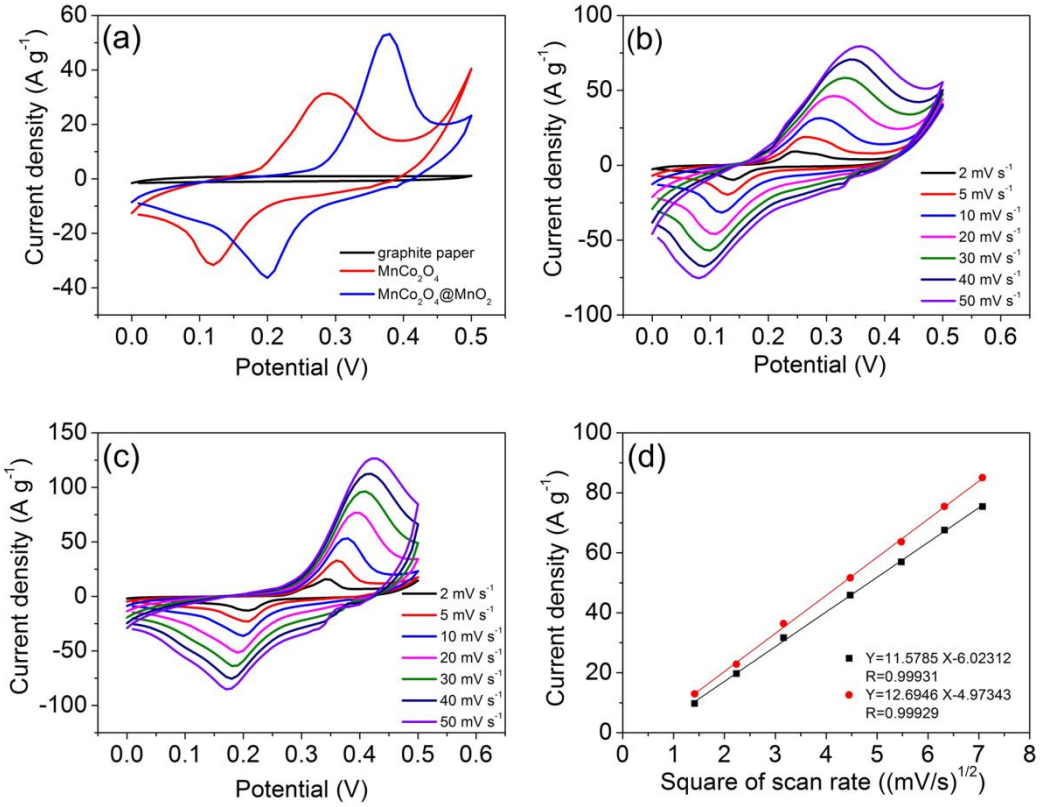
(a)
Current density (A g-1)
Potential (V)
graphite paper
MnCo2O4
MnCo2O4@MnO2
(b)
Current density (A g-1)
Potential (V)
2 mV s-1
5 mV s-1
10 mV s-1
20 mV s-1
30 mV s-1
40 mV s-1
50 mV s-1
(c)
Current density (A g-1)
Potential (V)
2 mV s-1
5 mV s-1
10 mV s-1
20 mV s-1
30 mV s-1
40 mV s-1
50 mV s-1
(d)
Current density (A g-1)
Square of scan rate ((mV/s)1/2)
Y=11.5785 X-6.02312
R=0.99931
Y=12.6946 X-4.97343
R=0.99929

3

4

Fig. 6

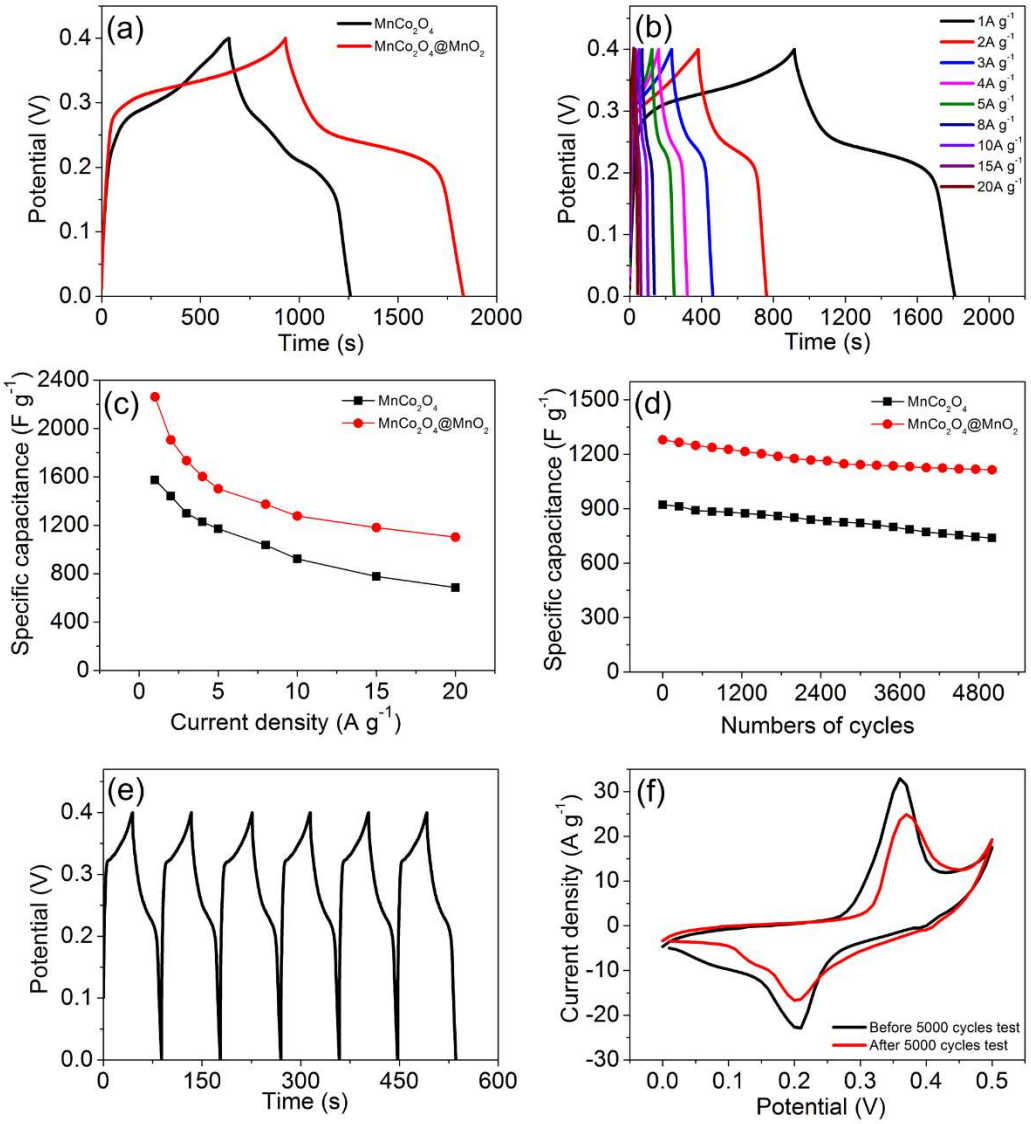
(a)
MnCo2O4
MnCo2O4@MnO2
Potential (V)
Time (s)
(b)
1A g-1
2A g-1
3A g-1
4A g-1
5A g-1
8A g-1
10A g-1
15A g-1
20A g-1
Potential (V)
Time (s)
(c)
MnCo2O4
MnCo2O4@MnO2
Specific capacitance (F g-1)
Current density (A g-1)
(d)
MnCo2O4
MnCo2O4@MnO2
Specific capacitance (F g-1)
Numbers of cycles
(e)
Potential (V)
Time (s)
(f)
Current density (A g-1)
Before 5000 cycles test
After 5000 cycles test
Potential (V)

Fig. 7

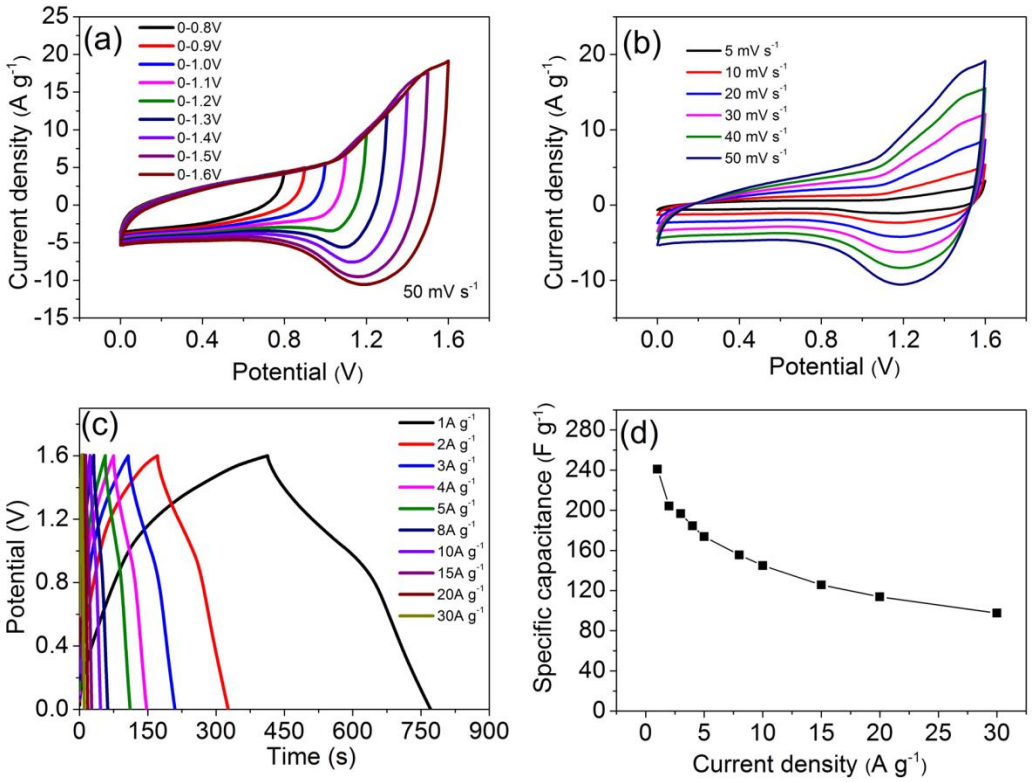
(a)
0-0.8V
0-0.9V
0-1.0V
0-1.1V
0-1.2V
0-1.3V
0-1.4V
0-1.5V
0-1.6V
50 mV s-1
Current density (A g-1)
Potential (V)
(b)
5 mV s-1
10 mV s-1
20 mV s-1
30 mV s-1
40 mV s-1
50 mV s-1
Current density (A g-1)
Potential (V)
(c)
1A g-1
2A g-1
3A g-1
4A g-1
5A g-1
8A g-1
10A g-1
15A g-1
20A g-1
30A g-1
Potential (V)
Time (s)
(d)
Specific capacitance (F g-1)
Current density (A g-1)

Fig. 8

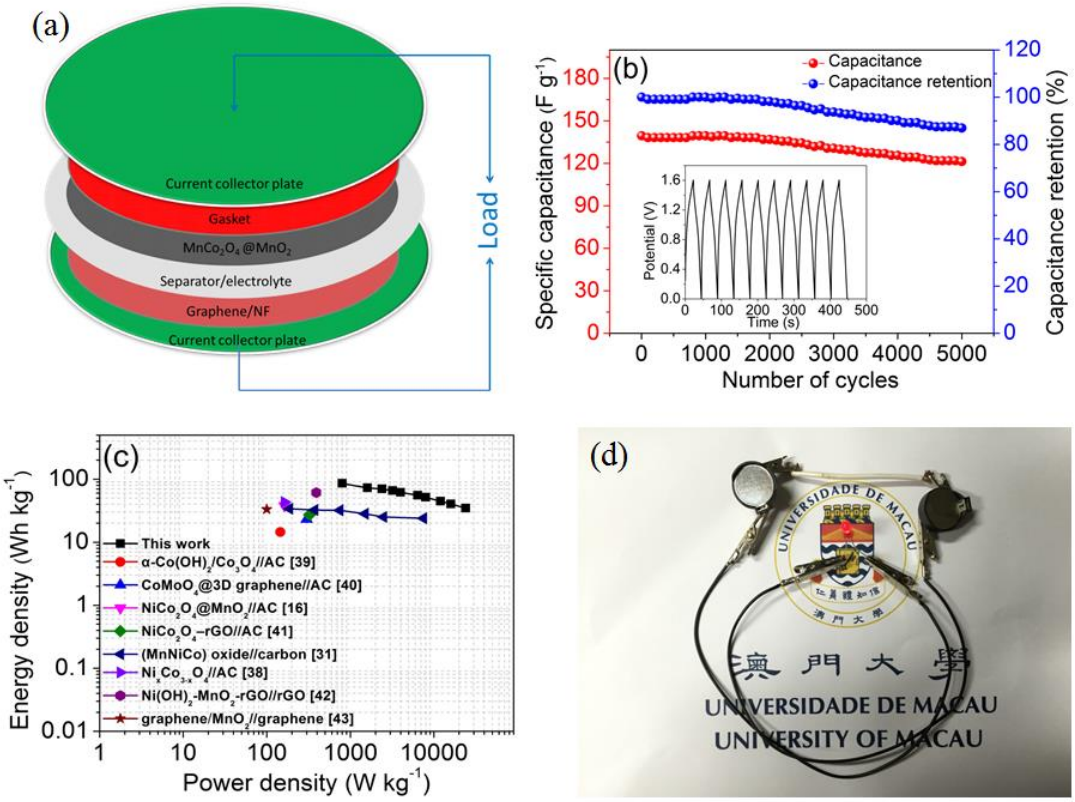
(a)
Current collector plate
Gasket
$MnCo_2O_4$@MnO_2
Separator/electrolyte
Graphene/NF
Current collector plate
Load
(b)
Capacitance
Capacitance retention
Specific capacitance (F g^{-1})
Capacitance retention (%)
Number of cycles
Potential (V)
Time (s)
(c)
Energy density (Wh kg^{-1})
Power density (W kg^{-1})
This work
α-Co(OH)$_2$/Co$_3$O$_4$//AC [39]
CoMoO$_4$@3D graphene//AC [40]
NiCo$_2$O$_4$@MnO$_2$//AC [16]
NiCo$_2$O$_4$–rGO//AC [41]
(MnNiCo) oxide//carbon [31]
Ni$_x$Co$_{3-x}$O$_4$//AC [38]
Ni(OH)$_2$-MnO$_2$-rGO//rGO [42]
graphene/MnO$_2$//graphene [43]
(d)
UNIVERSIDADE DE MACAU
UNIVERSITY OF MACAU